

A framework for estimating the anthropogenic
part of Antarctica’s sea level contribution in a
synthetic setting

Alexander T. Bradley^{1*}, David T. Bett¹, Paul R. Holland¹,
C. Rosie Williams¹, Robert J. Arthern¹, Jan De Rydt²

^{1*}British Antarctic Survey, Cambridge, United Kingdom.

²Department of Geography and Environmental Sciences, Northumbria
University, Newcastle upon Tyne, United Kingdom.

*Corresponding author(s). E-mail(s): aleey@bas.ac.uk;

Abstract

The relative contributions of anthropogenic climate change and internal variability in sea level rise from the West Antarctic Ice Sheet are yet to be determined. Even the way to address this question is not yet clear, since these two are linked through ice-ocean feedbacks and probed using ice sheet models with substantial uncertainty. Here we demonstrate how their relative contributions can be assessed by simulating the retreat of a synthetic ice sheet setup using an ice sheet model. Using a Bayesian approach, we construct distributions of sea level rise associated with this retreat. We demonstrate that it is necessary to account for both uncertainties arising from both a poorly-constrained model parameter and stochastic variations in climatic forcing, and our distributions of sea level rise include these two. These sources of uncertainty have only previously been considered in isolation. We identify characteristic effects of climate change on sea level rise distributions in this setup, most notably that climate change increases both the median and the weight in tails of distributions. From these findings, we construct metrics quantifying the role of climate change on both past and future sea level rise, suggesting that its attribution is possible even for unstable marine ice sheets.

Keywords: ice-sheets, ice shelves, Antarctica, ice-ocean interactions, attribution

001
002
003
004
005
006
007
008
009
010
011
012
013
014
015
016
017
018
019
020
021
022
023
024
025
026
027
028
029
030
031
032
033
034
035
036
037
038
039
040
041
042
043
044
045
046

047 Introduction

048
049 The West Antarctic Ice Sheet (WAIS) has undergone dramatic changes over the satel-
050 lite era, characterized by ice acceleration [1], thinning [2], retreat [3], and ice loss [4].
051 The WAIS currently contributes approximately 10% of global sea level rise (SLR) [5, 6]
052 and could add tens of centimeters over the coming decades, possibly dominating by
053 the end of the century [7]. However, despite being key symbols of anthropogenic cli-
054 mate change [8, 9], Antarctic ice loss, and thus associated SLR contributions, are yet
055 to be formally attributed to anthropogenic climate change [10].

056 A robust causal relationship between WAIS ice loss and anthropogenic climate
057 change is yet to be established because of strong internal variability in the region's
058 climate as well as ice-ocean feedbacks which perpetuate ice loss [10]. There are several
059 lines of evidence highlighting their complex interplay. While WAIS retreat was initi-
060 ated in the 1940s [11–13], after an approximately 10,000-year quiescent period [14],
061 anthropogenic influence on key climatological drivers in the region only became signif-
062 icant in the 1960s [15]. This suggests that the trigger for retreat would have occurred
063 even without anthropogenic forcing. Following its initiation, WAIS retreat was likely
064 sustained by ice-ocean feedbacks [16–21] (figure 1). Most notably, retreat of this marine
065 ice sheet across a retrograde bed (upward sloping in the flow direction) is associ-
066 ated with increased ice flux across the grounding line (where the ice transitions from
067 sitting on bedrock to a floating ice shelf), which promotes further retreat [22, 23]
068 (figure 1). Thus, one possibility is that the ongoing ice loss was triggered naturally in
069 the 1940s and retreat is dominated by self-perpetuating feedbacks, playing out on the
070 long timescales on which ice-sheets evolve [11, 13, 15, 24]. However, this retreat can-
071 not be purely self-sustaining, independent of external forcing, because ice discharge
072 remains responsive to ocean variability [25–27]. This picture is further complicated by
073 a proposed centennial scale warming of the Amundsen Sea [24, 28], which is partly
074 attributed to anthropogenic changes in large-scale climate systems [15, 28–30]. While
075 all of these processes may contribute to the ongoing ice loss, the relative contributions
076 of a historical trigger, ice-ocean feedbacks, and changes in climatic forcing are still
077 unknown.

078 Determining the role of anthropogenic climate change in SLR from the WAIS is
079 important for providing causal evidence to support recourse for the myriad social [e.g.
080 31], economic [e.g. 32], and ecological [e.g. 33] impacts of SLR, which are borne pri-
081 marily by poorer and low-lying island nations [34]. This is particularly pertinent in
082 light of the recent outcomes of the COP27 conference, in which a loss and damage fund
083 was established to compensate countries for the harm inflicted by anthropogenic cli-
084 mate change. In addition, attribution (or lack thereof) has implications for the future
085 of the WAIS: if the observed ice loss is due solely to internal variability and ice-ocean
086 feedbacks, SLR is likely already committed and irreversible; whereas, a significant
087 anthropogenic component might suggest that ongoing contributions strongly depend
088 on future greenhouse gas emissions.

089 Despite the importance of this question, an outline of how to address it is not yet
090 clear. Progress has been made towards such by ref. [35], who considered how ice sheet
091 retreat from a local topographic high under variable forcing may be attributed, using
092 a one dimensional ice sheet model. Using a set retreat threshold as the event to be

detected, they showed that while an observation of large retreat under a single realization of stochastic climatic forcing does not necessarily indicate that anthropogenic climate change was present in the forcing (figure 1), even modest anthropogenic trends in forcing make retreat more likely when averaged over multiple realizations. They conclude that a probabilistic approach, with multiple realizations of forcing, must be taken if robust attribution statements are to be made. Additionally, they showed that model parameter choices have a large impact on the likelihood of retreat, and thus the attribution statement; this suggests that multiple model parameters should be considered simultaneously in the attribution assessment, particularly when these are poorly constrained.

Here, we consider how the anthropogenic component of SLR contributions from WAIS may be determined, which uses a Bayesian approach integrating multiple realizations of forcing; we build upon ref. [35] in two main ways: firstly, we consider SLR contributions, rather than retreat, as the metric to be attributed. By using SLR as the attribution metric, we are able to quantify the role of anthropogenic climate change for observed SLR within any interval, rather than only exceedance of a single, pre-defined retreat threshold. This alleviates the common event definition problem which commonly impacts attribution studies [36]. Secondly, we explicitly account for the role of variable model parameters in the attribution assessment. Bayesian approaches naturally permit the joint probability density of multiple model parameters, which may be poorly constrained in general, to be represented within a projection of SLR [37]. This avoids the need to specify the precise values of model parameters at the outset, which yield very different attribution results depending on the particular choice of parameters in the framework of ref. [35].

More specifically, we consider parameter variability in the parametrization of ice shelf basal melting, which is calibrated by comparing the resulting ice shelf basal melt rate fields with output from a more detailed ocean model. This procedure represents a hybrid approach that sits between parametrizations of basal melting and coupled ice-ocean models, and calibrates melting directly, rather than only indirectly via its effect on ice flow. We demonstrate how the anthropogenic component of SLR contributions may be determined by considering the retreat of a synthetic marine-terminating ice sheet, which is highly susceptible to ice-ocean feedbacks and subject to forcing with strong internal variability, the characteristic features that are thought to obscure signals of anthropogenic climate change in SLR contributions from the WAIS. We demonstrate how uncertainties associated with poorly constrained model parameters interact with uncertainties associated with stochastic climate forcing, identifying that it is necessary to consider both, a feature that is lacking in current SLR projections. To the best of our knowledge, this is the first time such uncertainties have been considered simultaneously in an ice sheet modelling exercise.

We explicitly construct distributions of SLR which simultaneously account for parametric uncertainty (that arising from poorly constrained model parameters) and aleatory uncertainty (that arising from an ice sheet's variable response to different realizations of stochastic forcing). These distributions also reveal characteristic signatures of anthropogenic forcing on distributions of SLR from marine ice sheets, which

139 we describe, and allow us to construct a metric describing the influence of anthro-
140 pogenic forcing on SLR in this system. We conclude that even in highly unstable
141 marine ice sheets, the impact of anthropogenic forcing is detectible in principle, given
142 sufficiently large simulation ensembles as well as a full treatment of model param-
143 eter uncertainty. We finish with a brief discussion of the challenges associated with
144 determining the role of anthropogenic forcing on SLR contributions from the WAIS,
145 which are avoided in our use of a synthetic configuration. These include uncertainty in
146 other model parameters, uncertainty in the initial state, and uncertainties in climatic
147 forcing.

148

149 **Results**

150

151 **Interactions between aleatory and parametric uncertainties in** 152 **sea level rise projections**

153

154 We adopt a Bayesian approach in which parametric and aleatory uncertainties are
155 simultaneously accounted for. As is standard, parametric uncertainty is accounted
156 for by performing multiple simulations with different model parameters spanning the
157 parameter space (for each realization of forcing), with the resulting SLR contributions
158 weighted according to the level of agreement between a simulated quantity and its
159 ground truth [e.g. 38–43]. It is straightforward to incorporate aleatory uncertainty into
160 such an approach (see methods) by placing no preference on the specific realization of
161 forcing. Although accounting for parametric uncertainty in this way is now standard,
162 no study has yet probed the interaction between parametric and aleatory forcing
163 uncertainties, primarily because of the computational expense of doing so [40], since
164 multiple simulations with different model parameters must be run for each additional
165 realization of forcing.

166 To illustrate the approach, we focus on parametric uncertainty arising from the use
167 of a parametrisation of ice shelf basal melting. Parameterisations of basal melting are
168 often used instead of coupled-ice ocean models to reduce computational expense (in
169 coupled ice-ocean models, the ocean component typically represents the vast major-
170 ity of the expense [44]). Coupled ice-ocean models remain computationally intractable
171 for the large ensembles of simulations [44] required to incorporate both aleatory and
172 parametric uncertainty. However, parameterisations of melting neglect processes that
173 have been shown to be important in determining basal melting [e.g. 16, 45, 46], and
174 simulations employing parameterisations have been shown to yield basal melt rates
175 which result in poor skill at reproducing observed grounding line retreat [47] and ice
176 loss [48–50], compared to coupled ice-ocean models. Our approach can be considered
177 a hybrid between a parametrisation of melting and a coupled ice-ocean model: we use
178 a parameterisation of basal melting for computational efficiency and adopt a Bayesian
179 approach to the model parameters within: simulations are weighted by comparing
180 their predictions of basal melt rates with those from an offline ocean model at differ-
181 ent snapshot times throughout a simulation (methods); the ocean model thus plays a
182 role analogous to a ground-truth in a traditional Bayesian update, i.e. it is the infor-
183 mation assimilated into the model. It should be noted that this is a slightly different
184 philosophy to a typical Bayesian update in ice sheet modelling, in which agreement

with satellite observations, rather than with results of more detailed models, are typically used to update probabilities. We employ a common melt rate parameterisation in which melting has a quadratic dependence on ocean temperature and scales linearly with a dimensionless parameter M , which is independent of the ocean temperature (methods). The melt rate calibration procedure is only capable of calibrating the melting aspects of the flow model; other parameters, such as those related to basal sliding and ice viscosity, which are important in determining ice flow (and thus SLR) are not calibrated. Other studies [e.g. 38–43] have established procedures for calibrating many such aspects of ice-sheet models using observational data; the novelty of our calibration method is that it permits precise calibration of basal melt rates, which have, to the best of our knowledge, only previously been indirectly calibrated via the effect of melting on ice flow. In practice, all parameters with an important effect on ice dynamics should be calibrated (see ‘Discussion’), but our use of a generic ice sheet configuration (described below) allows us to neglect them, and focus on errors arising purely from poor melt rate parametrisation skill.

Our example configuration features a prominent seabed ridge (figure 2a) on which the ice shelf is stably grounded (figure 2b) during an initialization stage with temporally constant ocean forcing, corresponding to typical conditions in the Amundsen Sea offshore of the WAIS (methods). This grounding line position, located at a topographic high, is reminiscent of the WAIS configuration prior to the 1940s [11] and renders the system highly sensitive to ice-ocean feedbacks once grounding line retreat has been initiated [49]. We consider evolution from this steady state under variable ocean forcing, which is imposed by varying the depth of the pycnocline in the ambient ocean conditions (figure 2c–d). The ocean forcing includes a stochastic internal variability component, which mimics the observed amplitude [51, 52] and persistence [35] of internal variability in ocean conditions in the Amundsen Sea on decadal and interdecadal timescales. Superimposed on this forcing is either an anthropogenic trend – a 100 m/century linear shallowing of the pycnocline, illustrating a plausible historical anthropogenically driven trend in Amundsen Sea conditions [28, 53] – or no trend, representing the counterfactual scenario in which no anthropogenic climate change has taken place (figure 2g). For both of these scenarios (referred to as anthropogenic and counterfactual, respectively), we perform simulations with 40 independent realizations of forcing (the realizations in each of the two ensembles are also independent). Although accumulation rates also feature notable interdecadal internal variability, and are projected to display an anthropogenic trend in the future [7], this variability is smaller than in the ocean forcing for WAIS. In addition, changes in melting, rather than accumulation, are understood to have been the dominant driver of recent WAIS retreat [54, 55], and having multiple forcings, each with a unique anthropogenic trend complicates the attribution task somewhat.

For each realization of forcing, we perform simulations sampling the parameter space of M . Requiring that the ice shelf remains stably grounded at the ridge crest during the initialization phase, and retreats under forcing corresponding to the warmest observed conditions applied constantly, restricts us to considering the range $0.5 < M < 1.5$ (methods); we sample this range by taking $M \in \{0.5, 0.75, 1.0, 1.25, 1.5\}$. Thus, the total number of simulations is 400 (2 ensembles \times 40 members \times 5 M values).

231 Examining the response to a single illustrative realization of forcing (figure 2e),
232 for different melt parameters M , highlights the interplay between stochastic forcing
233 and parameter variability, elucidating the inextricable relationship between aleatory
234 and parametric uncertainty. On the centennial scale, this realization of forcing fea-
235 tures two prominent warm periods (figure 2e). During the first warm period (between
236 approximately $t = 20$ and $t = 40$ years), retreat is triggered in those simulations with
237 the largest values of M ($M = 1, 1.25, 1.5$; figure 2f). These retreats are initiated
238 towards the end of the first warm period (figure 2f), when the time-integrated melt
239 anomaly has caused enough ice shelf thinning to reduce ice shelf buttressing to the
240 level at which retreat is initiated. Accordingly, retreat is initiated soonest in the simu-
241 lation with the largest melt parameter M (figure 2f), which has the highest melt rates
242 and thus accumulates the time-integrated melt anomaly most rapidly. Once initiated,
243 retreat proceeds at a rate approximately independent of forcing (figure 2f), suggest-
244 ing that, once triggered, retreat is set primarily by ice-ocean feedbacks, although it
245 remains weakly responsive to changes in forcing. Simulations with smaller M (lower
246 melting) remain grounded at the ridge crest during the first warm period. Retreat is
247 initiated in the $M = 0.75$ simulation during the second warm period, again towards
248 the end of the period. A simulation with the same realization of forcing but with the
249 anthropogenic trend removed, and $M = 0.75$, does not retreat during this period (note
250 that this simulation is outside the ensemble structure outlined above, for which anthro-
251 pogenic and counterfactual ensembles are independent): the integrated melt anomaly
252 required to initiate retreat is achieved more easily during a given time period if there
253 is an anthropogenic trend in the forcing, than if not.

254 Under the same realization of forcing, SLR may be highly non-linear in M
255 (figure 2h). For example, SLR contributions in the highlighted curve in figure 2h
256 increase by 1800% (from 0.15 mm to 2.91 mm after 100 years) when the melt rate
257 parameter is increased from $M = 1$ to $M = 1.25$. This strong sensitivity demon-
258 strates the necessity of considering a range of parameter values in determining SLR
259 contributions, particularly when the system is susceptible to ice-ocean feedbacks, or
260 so-called tipping points may be passed. Furthermore, there are simulations in the
261 anthropogenic ensemble which yield lower SLR than simulations in the counterfac-
262 tual ensemble (figure 2h), and this behavior is strongly influenced by the value of M .
263 Thus, an observation of high SLR under a single realization of forcing is not neces-
264 sarily an indicator of strong anthropogenic influence (figure 1). Taken together, these
265 results – a strong sensitivity to the parameter M and to the specific realization of forc-
266 ing – demonstrate that parametric and aleatory uncertainty must be simultaneously
267 accounted for in SLR distributions, and thus any framework attempting to determine
268 the role of anthropogenic trends in forcing in them.

269 The non-linearity of SLR in M also demonstrates how single-point parameter cal-
270 ibration (where the set of model parameters are specified based on agreement with a
271 single metric, say the total melt flux out of an ice shelf cavity) may be problematic.
272 Such single-point calibrations are often applied when tuning melt rate parameterisa-
273 tions [e.g. 50, 56, 57]. In the example presented here, the mean melt rate at the start of
274 the simulation (at the end of the initialization stage, which is performed separately for
275
276

different values of M) is only weakly dependent on the melt rate parameter M (supplementary figure 3d), owing to a feedback between melting and ice geometry (methods). As a result, a small change in the single target metric to be matched would result in a large change in the selected value of M (supplementary figure 3d), which would ultimately result in a large change in the simulated SLR at the end of the simulation (figure 2h). In other cases where the target metric is more sensitive to parameters, a small change in the target metric would be expected to result in a small change in the selected parameter, but this may also ultimately result in a large change in the simulated SLR at the end of the simulation, owing to the non-linearity of SLR in M .

Influence of anthropogenic forcing on sea level rise probability distributions

Applying the Bayesian melt rate calibration procedure (methods), yields, for each time in each simulation, a distribution of SLR associated with the particular realization of forcing applied (supplementary figure 4). Then, by marginalizing over the realizations of forcing (methods), we obtain calibrated probability distributions of SLR for both anthropogenic and counterfactual ensembles, at each time (figure 3a).

The time evolution of both ensembles display qualitatively similar behavior. The evolution of the distributions can be categorized into two temporal parts: ‘tail emergence’ and ‘shift towards tails’ (figure 3c). At early times, the distributions are symmetric (figure 3a), with low skewness (figure 3c) reflecting retreat having not been triggered in any simulations. As retreat begins to be triggered in individual simulations, the ‘tail emergence’ period begins: a tail emerges (skewness increases, figure 3c), supported by increasing SLR contributions from those already retreating simulations, and kurtosis increases (figure 3d), indicating that the relative weight in the tails is reducing (kurtosis quantifies the proportion of weight placed in the tails, with low kurtosis corresponding to heavy tails). The timescale on which the tails emerge depends on the forcing (see below). Median SLR remains small in the tail emergence period (figure 3b).

As retreat is triggered in an increasing number of ensemble members, weight begins to shift to the tails; the ‘shift towards tails’ period begins when skewness and kurtosis reach a maximum (figure 3c–d). Beyond this maximum, weight moves towards the tails (kurtosis reduces, figure 3d) and, in response to this, the median increases (figure 3a), continuing to the end of the simulation. (The median is a more appropriate metric than the mean given the skewed data.) Both medians display a non-linear evolution, reflecting non-linear SLR contributions in individual simulations once retreat has been initiated. Although the precise details of the evolution of the distributions depends on both the system and the forcing (see below), we expect that this qualitative behavior is generic in marine ice sheets with tipping points under high variability stochastic forcing.

Despite these qualitative similarities between the anthropogenic and counterfactual distributions, there are clear quantitative differences, which highlight the importance of the anthropogenic trend in forcing. Firstly, the tail emerges sooner in the anthropogenic ensemble (figure 3c), because retreats are initiated sooner when a trend in

323 forcing is imposed (supplementary figure 1). This is despite the anthropogenic addi-
324 tional forcing being zero at the start of the simulation (figure 2g), highlighting the role
325 played by increases in forcing during the time period in which the destabilizing inte-
326 grated melt anomaly is accumulating; if forcing did not change over this period (or,
327 if the changes did not matter), the first retreats would take place at approximately
328 the same time in both ensembles. This is consistent with [15], who suggest that the
329 current retreat of WAIS was triggered naturally in the 1940s, but may have subse-
330 quently failed to recover due to increasing influence of anthropogenic forcing towards
331 the start of the 1960s. Secondly, the maximum skewness is lower, and achieved sooner,
332 in the anthropogenic case (figure 3c). In a given time period, retreat is triggered in
333 a greater proportion of simulations in the anthropogenic ensemble than in the coun-
334 terfactual ensemble (supplementary figure 1), resulting in probability distributions
335 shifting more quickly towards the heavy-tailed regime. This difference in retreat rate
336 triggering is because, as time proceeds, melt anomalies under anthropogenic forcing
337 become increasingly large, so a shorter positive anomaly duration is required to initiate
338 retreat. More specifically, with a linear anthropogenic trend, the time-integrated melt
339 anomaly scales with the square of time, which rapidly outweighs any time-integrated
340 negative internal component: the system is more vulnerable to long-lasting trends in
341 melting than to short term variability. Finally, and most importantly, on the centennial
342 timescale, both the median is larger, and the kurtosis smaller, in the anthropogenic
343 ensemble than in the counterfactual ensemble; i.e. not only does anthropogenic forcing
344 increase the median of the distribution, it also results in greater weight in the tails:
345 extreme events, with high SLR contributions, have relatively large probabilities in the
346 anthropogenic ensemble. This emphasizes the need to consider the shape, as well as
347 the spread (e.g. the variance), when communicating how emissions pathways affect
348 future SLR scenarios with policymakers.

349 Figures 3b-d also indicate how summary statistics differ between the calibrated and
350 uncalibrated distributions, with the latter obtained by setting the posterior probability
351 equal to the prior probability (methods), i.e. all values of M are weighted equally. In
352 both ensembles, parametric calibration of M has an important effect on the median,
353 evidencing the need to apply parametric calibration in projections of SLR from ice
354 sheets. Reduced uncertainty in projections is often (perhaps implicitly) cited as a key
355 benefit of parametric calibration [e.g. 38, 40]; whilst our simulations provide evidence
356 to support this, displaying increased kurtosis (reduced weight in the tails; figure 3d)
357 in the calibrated case, there remain large uncertainties in calibrated distributions
358 (figure 3a). This suggests that aleatory uncertainty is an unavoidably large part of
359 uncertainty in projections of SLR from ice sheets, particularly those highly susceptible
360 to ice-ocean feedbacks, and cannot be neglected: parametric calibration alone is not
361 sufficient, and there is irreducible uncertainty in SLR from marine ice sheets.

362 363 **Quantifying signals of anthropogenic trends in forcing** 364

365 The role of anthropogenic climate change in individual weather events is often framed
366 as an anthropogenic enhancement [36]: how many times more (or less) likely was the
367 event made by anthropogenic climate change? Having constructed distributions of SLR
368 in both anthropogenic and counterfactual cases, the ratio of these – the anthropogenic

enhancement ratio (AER) – naturally emerges as a metric to quantify how many times more likely an observed SLR was made by the presence of an anthropogenic trend in forcing, and go beyond the qualitative comparisons of the previous section. An AER of 2, for example, indicates that anthropogenic forcing made a given SLR contribution 100% more likely (or, equivalently, twice as likely). The AER for our ensembles is shown in figure 4a, where values along each line of constant time represent the ratio between the anthropogenic and counterfactual probability distributions (as shown for specific times in figure 3a). Note that, because the AER can be constructed for any time throughout the simulation, past and future SLR are equally applicable – the present has no special status. Therefore, attribution statements may be made for either past or future SLR contributions (or both).

There is a band in which the AER is infinite, which is caused by the tails of the anthropogenic distribution extending to higher SLR values than those in the counterfactual distribution (figure 4a). An observation of SLR in this band would have been impossible without anthropogenic climate change—no counterfactual simulations produce this value. The band spreads out in time from an area close to the origin (recall that the tail of the anthropogenic distribution emerges soon after the start of the simulation) at a rate that is set by the retreat of the individual simulation with the highest SLR.

The AER is generally increasing in SLR, indicating that a higher SLR over many realizations of forcing is a stronger indicator of anthropogenic climate change. This demonstrates the importance, and value, of accounting for aleatory uncertainty: under a single realization of forcing, higher SLR does not necessarily indicate a strong influence of anthropogenic climate change (figure 1), but it does when appropriately averaged over many realizations of forcing. This also highlights the shift from a binary yes-no question, to a probabilistic approach, that necessarily takes place when accounting for aleatory uncertainty [35]. The AER has a slightly banded structure (figure 4a), which results from the finite size of our ensembles (in the limit of infinite ensemble members, the proportion of retreats initiated would be smooth, whereas because of the finite size of our ensemble, the proportion of retreats initiated oscillates around the trend in this quantity, with periods when relatively more, and periods when relatively few, retreats are initiated compared to the background trend, see figure 1). While we expect that the banding would disappear as the number of realizations of forcing goes to infinity, we note that increasing this number is particularly computationally expensive when accounting for aleatory and parametric uncertainty simultaneously.

In practice, observed SLR follows a single trajectory through this AER space, such as the selected simulations shown in figure 4b–d, in which retreat is triggered after approximately 20, 40, and 60 years, respectively (figure 4a). Their values are indicative of the clear signal of anthropogenic climate change: at the end of the simulation, AER is approximately 2.5, 3.9 and 2.2, respectively, corresponding to increases in probability of 150%, 290%, and 120%. Once retreat has been triggered, the AER remains fairly constant. It is worth noting that these values are perhaps modest compared to glaciological attribution studies applied to mountain glaciers [e.g. 58, 59]. This is a direct consequence of our choice of setup: we consider a scenario in which internal variability is relatively large compared to the anthropogenic trend and is highly susceptible

415 to ice-ocean feedbacks (and these selected trajectories don't enter the tail band, for
416 which $\text{AER} \rightarrow \infty$).

417 From a policy perspective, a third useful question, beyond how to address and
418 how to quantify the role of anthropogenic trends in forcing, is: what is the uncer-
419 tainty in this quantification? Having constructed distributions associated with each
420 realization of forcing (which the distributions shown in figure 3a are the mean over),
421 such uncertainties can be probed. To do so, we bootstrap values of the distributions
422 from individual realizations of forcing to determine a confidence interval (methods) –
423 a measure of the likely spread in AER – around our central estimates (figure 4b–d).
424 Uncertainty in AER is generally smaller along contours corresponding to later retreat
425 (figure 4b–d). This is commensurate with relatively few simulation trajectories enter-
426 ing the region in and around the tail band, leading to increased uncertainty: although
427 the central estimate of anthropogenic enhancement is itself largest in the tails, that
428 is where the uncertainty in the value is greatest. We expect that this error bound
429 would reduce with increasing numbers of realizations of forcing. Thus, we expect that
430 real world attribution studies will have to grapple with the limitation that increasing
431 ensemble size is required to reduce uncertainty in the role of anthropogenic forcing,
432 but to do so requires substantial additional computational resources.

433

434

435 Discussion

436

437 The example presented here provides a path towards assessing the role of anthro-
438 pogenic climate change in SLR contributions from the West Antarctic Ice Sheet,
439 including both quantifying the strength of the anthropogenic signal and its uncer-
440 tainty. Our use of a Bayesian framework allows us to treat parametric uncertainty
441 within attribution assessments and avoids the need to specify a single event to be
442 detected. By abstracting and considering a generic ice sheet, we are able to focus on
443 errors in melting, with the hope that the melt calibration approach may help to bridge
444 the considerable gap in fidelity to observations between parameterisations of melting
445 and coupled ice-ocean simulations.

446 Determining the precise influence of anthropogenic climate change on SLR con-
447 tributions from the WAIS requires simulations to be performed using geometries and
448 parameters that represent real world conditions. Here we identify three key classes
449 of problems which must be overcome in doing so: computational challenges, initial
450 state challenges, and challenges arising from uncertainty in climatic forcing. Computa-
451 tional challenges arise from the large number of simulations required to appropriately
452 account for parametric and aleatory uncertainty. In considering a generic marine ice
453 sheet, we are able to neglect uncertainty arising from model parameters governing
454 basal sliding and ice viscosity, as well as processes such as damage [e.g 19, 60], calv-
455 ing [e.g. 46, 61, 62], sliding law [e.g. 63], and ice rheology [e.g. 64] which might obscure
456 (or amplify) long-term climatic trends in the forcing, but should be included in assess-
457 ments of SLR and thus its attribution to anthropogenic climate change. Additional
458 parametric uncertainties can be succinctly integrated into the Bayesian approach taken
459 here [37], and should be calibrated with observations. The computational challenge
460 is particularly pertinent given that a high spatial resolution must be used to ensure

correct representation of ice sheet key processes [e.g. 65]. In addition, the effect of parameters which control the strength of Bayesian updates must be explored; although we find that varying these parameters within reasonable ranges does not qualitatively change the results (methods), they may influence the precise values of anthropogenic enhancement. It should also be noted that, ideally, multiple different ice sheet models should be used in order to assess structural uncertainties arising from those processes not represented in some ice sheet models [37], further adding to the computational challenge.

Determining the initial state – the configuration of the ice sheet prior to the era of anthropogenic influence – also represents an crucial challenge. Projections of ice sheet evolution are sensitive to their initial states, similar to numerical weather forecasts [66], but relatively little is known about the configuration of the WAIS prior to the satellite record beyond broad bounds on grounding line locations [11]. One particular challenge in this regard is determining the ice front position, which typically remains fixed in ice sheet models, but may have a strong impact on ice shelf buttressing and thus retreat potential. Additionally, ice sheet memory of Holocene conditions must be considered: here, we have assumed that the ice sheet is in steady state at the onset of a trend in forcing; in practice, however, there is evidence of a slow retreat of the WAIS over the Holocene [14]. Given the long timescales on which ice sheets fully respond to changes in forcing, knowledge of this state may be retained by the ice sheet, and thus affect the likelihood of retreat.

Finally, challenges associated with uncertainties in climatic forcing must be overcome. Here, we assumed that the anthropogenic trend is known and well characterized, but in practice this must itself be inferred from observations and models of climate, representing an attribution challenge in itself. For WAIS, this is complicated by the compound drivers of changes: ocean warming drives retreat, but trends in ocean warming are primarily driven by trends in winds [24]. Additionally, anthropogenic trends in accumulation, not considered in this study, must be considered simultaneously with trends in ocean warming; in the future, trends in accumulation are expected to partly offset ice loss from WAIS [7], potentially obscuring the anthropogenic signal.

The work presented here can be considered as a framework for producing calibrated distributions of SLR, in addition to their application to attribution statements. We have demonstrated that both aleatory and parametric uncertainty are important components of ice sheet SLR projections, and suggest that future assessments of SLR from ice sheets must account for these sources of uncertainty. As we have shown, parametric calibration reduces uncertainty, but the susceptibility to ice-ocean feedbacks renders broad distributions inevitable [67]: much like other aspects of the climate system [68], ice sheets have irreducible uncertainty. The glaciological community must become more comfortable with these fundamental aspects of uncertainty and appropriately communicate them to policy-makers and stakeholders.

By constructing calibrated distributions of SLR contributions, we showed that anthropogenic climate change increases both the median of distributions, and the relative weight of their tails: much like many other weather events [69], even modest anthropogenic climate change can make extreme scenarios many times more likely.

507 Using these distributions, we constructed a metric to quantify the role of anthro-
508 pogenic forcing, concluding that even in highly unstable marine ice sheets, the impact
509 of anthropogenic forcing is detectable in principle, given sufficiently large simulation
510 ensembles forced by profiles with and without an anthropogenic trend, as well as a
511 full treatment of model parameter uncertainty. In other words, attribution studies are
512 tractable for the WAIS. The implications of attributing ice loss from the WAIS, both
513 for the harms caused by SLR, and the implications for the future of the WAIS, provide
514 strong motivation to pursue such studies.

515

516 Data availability

517

518 Data used to generate figures contained herein is contained in an open GitHub repos-
519 itory at <https://github.com/alexbradley/WAISAttribution-figures>, which is held in
520 permanent Zenodo repository at [10.5281/zenodo.10514080](https://zenodo.org/record/7900762#.ZFUykOzMLPa). Processed ice sheet and
521 ocean model data is contained in a permanent Zenodo repository at [https://zenodo.](https://zenodo.org/record/7900762#.ZFUykOzMLPa)
522 [org/record/7900762#.ZFUykOzMLPa](https://zenodo.org/record/7900762#.ZFUykOzMLPa).

523

524 Code availability

525

526 Code to analyze data is contained in an open GitHub repository at [https://github.](https://github.com/alexbradley/WAISAttribution-figures)
527 [com/alexbradley/WAISAttribution-figures](https://github.com/alexbradley/WAISAttribution-figures), which is held in permanent Zenodo repos-
528 itory at [10.5281/zenodo.10514080](https://zenodo.org/record/7900762#.ZFUykOzMLPa).

529

530 Competing interests

531

532 The authors declare no competing interests.

533

534 1 Author Contributions

535

536 A.T.B. performed the model simulations, analysed the results and drafted the
537 manuscript. D.T.B. and P.R.H. assisted with the development of the ocean model
538 configuration. C.R.W. and R.J.A. assisted with the development of the ice sheet
539 model configuration. P.R.H., C.R.W., and R.J.A. supervised the project. All authors
540 assisted with the conception of the study and provided feedback and comments during
541 editing.

542

543 2 Acknowledgements

544

545 A.T.B., D.T.B., P.R.H., C.R.W., R.J.A are supported by the NERC Grant
546 NE/S010475/1. A.T.B., D.T.B., P.R.H are supported and the PROTECT project,
547 which received funding from the European Union’s Horizon 2020 research and inno-
548 vation programme under grant agreement no. 869304. J.D.R. is supported by the
549 TiPACCs project, which receives funding from the European Union’s Horizon 2020
550 research and innovation programme under grant agreement no. 820575. J.D.R. was
551 supported by a UKRI Future Leaders Fellowship (MR/W011816/1). This work used
552 the ARCHER2 UK National Supercomputing Service (<https://www.archer2.ac.uk>).

Methods

Sea level rise contributions accounting for parametric and aleatory uncertainty

For a given trend in forcing, denoted \mathcal{F} , (i.e. after specifying whether the trend is anthropogenic or counterfactual), the probability of a given SLR, ΔSLR , accounting for aleatory and parametric uncertainty may be expressed as [37]

$$P(\Delta\text{SLR}|\mathcal{F}, \mathcal{I}_0) = \frac{1}{n} \sum_{i=1}^n \int P(\Delta\text{SLR}|\mathcal{F}, \mathcal{N}, \mathcal{R}_i, \mathcal{I}_0) P(\mathcal{N}|\mathcal{R}_i, \mathcal{F}, \mathcal{I}_0) d\mathcal{N}. \quad (1)$$

Here, \mathcal{N} is the space of model parameters, n is the total number of realizations of forcing, \mathcal{R}_i is the specific realization of forcing (with i a dummy index), and \mathcal{I}_0 represents the initial conditions. The expression (1) follows from a first-principles probabilistic expression of SLR [37], after assuming that each specific realization of forcing has equal probability, $P(\mathcal{R}_i) = 1/n$, and that the initial state \mathcal{I}_0 is known. For our specific application of (1), \mathcal{N} is the space of melt rate parameters, $0.5 < M < 1.5$. Note that the expression (1) does not include any account of model structural uncertainty, which arises from the approximations that ice sheet models make, as well as their incomplete representation or omission of physical processes [37]. Such uncertainties can only be accurately probed by performing the same numerical experiments with an ensemble of different ice sheet models, typically in a model intercomparison exercise [e.g. 70] and is therefore beyond the scope of this work. (It should be noted that the WAVI ice sheet model used herein demonstrates good agreement with other state-of-the-art ice sheet models in the most recent ice sheet model intercomparison exercise [70].) Note that constructing distributions of SLR using the calibration procedure outlined below requires values of SLR to be known for all parameter values, but simulations provide only a finite amount of observations. Here, we obtain SLR as a function of M by linearly interpolating between individual M (see figure 4e).

Melt rate calibration

The calibration of model parameters M enters distributions of SLR through the probability $P(M|\mathcal{R}_i, \mathcal{F}, \mathcal{I}_0)$, which appears in (1) (here we use the specific parameter name M , rather than the generic name \mathcal{N}). Following a standard Bayesian approach, we assume a prior distribution on the parameters M (with hyperparameter μ), which is then updated as new information is assimilated through the likelihood. In our case, this assimilated information is melt rates from an offline ocean model (see below); denoting this information by \mathcal{O} , Bayes' rule states that

$$P(M|\mathcal{O}, \mu) = \frac{P(\mathcal{O}|M, \mu) P(M|\mu)}{P(\mathcal{O}|\mu)} \quad (2)$$

The first term in the numerator on the right-hand side of (2) represents a likelihood function, describing how the prior distribution (second term in the numerator on the

599 right-hand side) is updated to assimilate ocean model results. The prior distribution
600 describes the state of belief in model parameters N prior to comparison with the ocean
601 model. The left-hand side of (2) represents the posterior distribution – the distribution
602 of parameters M following assimilation of ocean model information. The denominator
603 of the right-hand side of (2) simply acts to normalize the probability distribution.

604 Here, we assume a Gaussian prior, which maximizes the relative entropy when only
605 estimates of the prior mean μ and standard deviation σ_P are available [71, 72]:

$$606$$

$$607 \quad P(M|\mu) = \frac{\alpha}{\sqrt{2\pi\sigma_P^2}} \exp\left(-\frac{|M - \mu|^2}{2\sigma_P^2}\right). \quad (3)$$

$$608$$

$$609$$

610 Here α is a normalization constant, which ensures that the distribution (3) integrates
611 to unity when initialization bounds on M are imposed (see ‘Ice Sheet Model Initializa-
612 tion’ below). σ_P can be thought of as describing the strength of confidence in the initial
613 estimate of M , which is centered about the hyperparameter μ : a low (high, respec-
614 tively) σ_P corresponds to high (low) confidence that the hyperparameter μ represents
615 the true value of M . In the results contained herein, we use $\mu = 1.25$, based on agree-
616 ment in the mean melt rate after the initialization stage (in this case, a mean melt rate
617 of 23 m year^{-1} , which can be thought of as an arbitrary piece of prior information). We
618 use $\sigma_P = 0.2$ (supplementary figure 4), representing somewhat weak confidence that
619 the value $M = \mu$ represents the true value of M . Supplementary figure 6b shows a plot
620 of the Gaussian prior (3) as a function of M for different values of σ_P with $\mu = 1.25$.

621 To determine the likelihood $P(\mathcal{O}|M, \mu)$, we first specify calibration timeslices $\tau =$
622 $\{\tau_1, \dots, \tau_n\}$ and, for each timeslice, run the ocean model in the geometry set by the
623 ice-only model. After doing so, we have two melt rate fields,

$$624$$

$$625 \quad \dot{m}_{\text{param}}^k = \dot{m}_{\text{param}}(x, y, t = \tau_k | M), \quad (4)$$

$$626$$

$$627 \quad \dot{m}_{\text{ocean-model}}^k = \dot{m}_{\text{ocean-model}}(x, y, t = \tau_k | M) \quad (5)$$

$$628$$

629 from the parameterisation of melting and from the ocean model, respectively, and
630 for each timeslice $k = 1, \dots, n$. (Note that the ocean model depends on the melt
631 rate parameter M via the ice-shelf cavity geometry.) A melt error functional D_j
632 is determined by comparing these two fields. The particular choice of the form of the D_j
633 is subjective, reflecting how melting should be penalized. Here, we take D_j to be the
634 mean absolute error in the two melt fields on grid cells below 500 m depth. This reflects
635 the fact that deep areas, typically close to grounding lines, have disproportionately
636 large impacts on the dynamics of the grounded ice [73–75].

637 From the timeslice errors D_j , we determine an average error $D = (1/n) \sum_{j=1}^n D_j$.
638 The likelihood is then determined from an exponential error model,

$$639$$

$$640 \quad P(\mathcal{O}|M, \mu) = \frac{1}{\sqrt{2\pi\sigma_L^2}} \exp\left(-\frac{D^2}{2\sigma_L^2}\right). \quad (6)$$

$$641$$

$$642$$

643 Here σ_L is a melt error covariance, which describes how harshly errors in the melt
644 rate from the parameterisation are penalized (with respect to the ocean model): for

low σ_L , errors are penalized more harshly, whereas for high σ_L , errors are penalized less harshly. In the limit $\sigma_L \rightarrow \infty$, each parameter value M is assigned equal weight, and the posterior distribution is identical to the prior (supplementary figure 4f). Supplementary figure 6b shows a plot of the exponential error model (6) as a function of D for different values of σ_L . In the results presented here, we use $\sigma_L = 10$ m/year. In general, the σ_L should be on the same order of magnitude as errors in melting; in our simulations, melt errors are typically on the order of 10s of meters per year (supplementary figure 4a).

To assimilate timeslice errors into the Bayesian update, we require $P(\mathcal{O}|M, \mu)$ as a function of M , but the simulation only provides sparse points (figure 4b). To overcome this, we interpolate between the data points using a smoothing spline fit, via the FIT function in MATLAB.

Supplementary figure 6c shows the AER as a function of SLR and time (i.e. as in figure 4 of the main text) for different values of the prior parameter σ_P and melt error covariance σ_L within reasonable ranges. We see that, while varying these parameters adjusts the precise value of the AER, the overall picture – that higher observed SLR are concomitant with stronger anthropogenic influence – remains. The small exception to this is for large σ_P and small σ_L , for which the anthropogenic signal is most obscured (see below) and a band of AER < 1 emerges close to the tail. This is a finite size effect, and would disappear in the limit of a large number of simulations, emphasizing the need for large ensembles of simulations.

For smaller σ_L , errors in melting are penalized more harshly; in this study, smaller σ_L tends to shift weight towards smaller M , which typically display smaller errors in melting (see supplementary figure 4a–b for an example from one realization of forcing). Simulations using a smaller value of M require a larger time-integrated forcing anomaly to achieve the same integrated melt anomaly required to initiate retreat. Simulations in which this is achieved in the anthropogenic case and not in the counterfactual case, tend, therefore, to be observed later on average, when the ensemble mean difference in forcing is greater. Thus, for a given time, the ratio of ensemble members which have retreated in the anthropogenic ensemble to those which have retreated in the counterfactual ensemble is closer to unity for smaller M , leading to a dampened anthropogenic effect. Conversely, smaller σ_P shifts weight towards $M = \mu = 1.25$ (in this case), which is at the higher end of the M range considered here, enhancing the anthropogenic effect.

Details of ice sheet configuration

The setup of the generic marine ice sheet configuration is very similar to that of [49], who interrogated how ice-ocean feedbacks perpetuate retreat of an ice sheet from a seabed ridge using a coupled ice-ocean model under constant forcing scenarios. In this setup, the bathymetry (figure 2a) can be expressed as the sum of along-flow and cross-flow components:

$$B(x, y) = B_x(x) + B_y(y), \quad (7)$$

691 where

692

693

694

695

696

697

$$B_x(x) = 400 \exp \left[-\frac{(x - 265 \times 10^3)}{2\sigma_b^2} \right] \text{ m}, \quad (8)$$

698

699

700

701

702

703

704

705

Here, x and y are co-ordinates in the along- and cross-flow directions, respectively (the ridge is aligned along the cross-flow direction, see figure 2a). The cross-flow bathymetry contribution, $B_y(y)$, corresponds to a symmetric valley-like configuration, whose margins are located 500 m below sea level and whose center is 1100 m below sea level; the along-flow bathymetry contribution, $B_x(x)$, corresponds to a Gaussian ridge with height 400 m and lengthscale $\sigma_b = 1.1 \times 10^4$ m, which is superimposed on the valley at a position centered on $x = 265$ km.

706

707

708

709

710

711

712

713

714

715

716

Following [49], ice rheology is described by Glen's law with flow exponent $n = 3$. A constant rate factor $A = 2.94 \times 10^{-9} \text{ a}^{-1} \text{ kPa}^{-3}$ is applied everywhere, except for within 5 km of the ice margins (i.e. for $y < -20$ km and $y > 20$ km), where the rate factor is set to $A = 5.04 \times 10^{-9} \text{ a}^{-1} \text{ kPa}^{-3}$; this is to mimic the narrow, low viscosity, shear margins which are characteristic of WAIS outlet glaciers, particularly Pine Island Glacier [76]. The sliding coefficient is set to $20 \text{ m a}^{-1} \text{ kPa}^{-1}$ everywhere. Surface accumulation varies linearly from 15 m a^{-1} at the ice divide ($x = 0$ km) to 1 m a^{-1} at $x = 150$ km and is set to a constant value of 1 m a^{-1} between $x = 150$ km and the ice front ($x = 300$) km. The resulting total surface accumulation, 67.5 Gt a^{-1} , closely matches observations [77], while the spatial pattern respects reduced accumulation with reducing altitude.

717

718

WAVI ice sheet model

719

720

721

722

723

724

725

726

727

SLR contributions are determined from simulations using the Wavelet-based Adaptive-grid Vertically-integrated Ice-sheet model (WAVI) [72, 78], a finite volume ice sheet model including a treatment of both membrane and simplified vertical shear stresses [79]. WAVI uses a regular solution grid (here 1 km in both directions), which is refined dynamically during the solution procedure to facilitate solution speed and accuracy. WAVI assumes a fixed ice front position, which is set to $x = 300$ km (this is equivalent to prescribing a calving law that the calving flux is equal to the normal ice velocity at the ice front).

728

729

Melt rate parameterisation

730

731

732

Melting in the ice sheet model is parameterized according to a quadratic temperature law [80],

$$\dot{m} = M\Gamma (T_a - T_f)^2. \quad (10)$$

733

734

735

736

Here, M is a (variable) dimensionless melt rate parameter, T_a is the ambient temperature far from the ice shelf base (see below), T_f is the local freezing temperature and $\Gamma = 0.56 \text{ m yr}^{-1} \text{ }^\circ\text{C}^{-2}$ plays the role of an exchange coefficient between temperature and melt rate. (Using the nomenclature of [50, 81], $\Gamma = \gamma_T[\rho_w c_p / (\rho_i L)]^2$, where

γ_T is an exchange velocity, ρ_w is water density, ρ_i is the ice density, c_p is the specific heat capacity of water, L is the latent heat of fusion). The formulation (10) essentially encodes two mechanisms which strongly affect ice shelf basal melting: (1) ice shelf melting is governed by the turbulent heat flux from the ocean to the ice, which varies like the product of ocean temperature and velocity; (2) ocean velocity increases with the local thermal forcing ($T_a - T_f$) as meltwater is released, increasing the buoyancy forcing and thus circulation strength. This parameterisation has been used in numerous ice sheet modelling studies [see 44, and references therein], including the latest ISMIP assessments [81].

As is standard, we assume that the local freezing point depends linearly on pressure and salinity, $T_f = \lambda_1 S_a + \lambda_2 + \lambda_3 z_b$, where $\lambda_1 = -5.73 \times 10^{-2} \text{ }^\circ\text{C}$ is the liquidus salinity slope, $\lambda_2 = 8.32 \times 10^{-2} \text{ }^\circ\text{C}$ is the liquidus intercept, $\lambda_3 = 7.61 \times 10^{-4} \text{ }^\circ\text{C m}^{-1}$ is the liquidus depth slope, S_a the ambient salinity (see below), and z_b is the depth of the ice shelf base.

We take a layered structure for the ambient temperature and salinity (figure 2c–d), parameterized solely via the depth of the pycnocline centre, P_c (which is in general time-dependent), and the pycnocline half-width w :

$$T_a(z; P_c, w) = \begin{cases} 1.2 & z < P_c - w \\ 1.2 - 2.2 \frac{z - (P_c - w)}{2w} & P_c - w \leq z \leq P_c + w \\ -1 & z > P_c + w \end{cases} \quad (11)$$

$$S_a(z; P_c, w) = \begin{cases} 34.6 & z < P_c - w \\ 34.6 - 0.6 \frac{z - (P_c - w)}{2w} & P_c - w \leq z \leq P_c + w \\ 34.0 & z > P_c + w \end{cases} \quad (12)$$

The profiles (11) and (12) are piecewise linear functions of depth (figure 2b): they are constant in both an upper (temperature -1°C , salinity 34 PSU, corresponding to Winter Water) and lower layer (temperature 1.2°C , salinity 34.6 PSU, corresponding to Circumpolar Deep Water), which are separated by a pycnocline of $2w$ m thickness, across which the temperature and salinity vary linearly. These piecewise linear profiles are approximations to typical conditions in the Amundsen Sea [26, 52]. Here, we take $w = 200$ m, corresponding to a pycnocline width of 400 m, which is consistent with observations [51, 52]. Time varying stochastic forcing is applied by varying the pycnocline center (see ‘Stochastic Forcing’ below).

MITgcm ocean model

Ocean model melt rates used as calibration data are calculated by resolving the ice shelf cavity circulation using the Massachusetts Institute of Technology General Circulation Model (MITgcm) [82]. The procedure applied to determine ocean model melt rates at timeslices τ_1, \dots, τ_n under a given forcing $P_c(t)$ is as follows: (1) run the ice sheet model (with parameterized melting) under this forcing profile; (2) use the output of this to determine ice shelf geometries at timeslices $t = \tau_1, \dots, \tau_n$; (3) for each of these geometries, run the ocean model in this geometry, with forcing applied via

783 a restoring boundary condition corresponding to the profiles $P_c(\tau_k)$. The restoring
 784 boundary condition is applied at the downstream end of the domain at $x = 360$ km
 785 (figure 2a), where the temperature and salinity are restored to vertical profiles T_a and
 786 S_a over a distance of five horizontal grid cells with a restoring timescale of 12 hours.
 787 An example of melt rates fields \dot{m}_{param}^k and $\dot{m}_{\text{ocean-model}}^k$ produced by this procedure
 788 is shown in figure 2.

789 The ocean model grid has 55 layers with a vertical spacing of $dz = 20$ m, and
 790 a horizontal resolution of $dx = 1$ km. We use the MITgcm in hydrostatic mode
 791 with an implicit nonlinear free surface scheme, a third-order direct space-time flux
 792 limited advection scheme, and a non-linear equation of state [83]. The Pacanowski-
 793 Philander [84] scheme parameterizes vertical mixing. Constant values of 15 and 2.5
 794 $\text{m}^2 \text{s}^{-1}$ are used for the horizontal Laplacian viscosity and horizontal diffusivity, respec-
 795 tively. The equations are solved on an f -plane with $f = -1.4 \times 10^{-4} \text{ s}^{-1}$. For each
 796 geometry, the MITgcm is run for three months, using a timestep of 30 seconds, after
 797 which the configuration is in quasi-steady state. The ocean model melt rate is taken
 798 as the melt rate after three months of the simulation. The drag coefficient in the
 799 three-equation formulation of melting [85] used in the MITgcm is taken to be 9×10^{-3} ;
 800 this value ensures that the ocean model melt rate in the post-initialization geometries
 801 (see ‘Ice Sheet Model Initialization’) closely matches observed total meltwater flux
 802 values [e.g. 52] from Pine Island Glacier.

803

804 Ice sheet model initialization

805

806 Following [49], we apply a two-stage initialization procedure, outlined in figure 3a. In
 807 the first initialization stage, the ice geometry is timestepped from an initial configu-
 808 ration in which the ice-surface is 150 m above sea level for 50 years (note that WAVI
 809 uses a hydrostatic flotation condition, so specifying the ice surface and bed elevation
 810 prescribes the ice thickness everywhere). Following this, the ice is approximately in
 811 steady state, with ice shelf geometry shown in figure 3c.

812 In the second stage of the initialization procedure, melting is turned on (figure 3).
 813 The ice geometry is then timestepped from that at the end of the first initialization
 814 stage for fifty years using a constant ocean forcing with $P_c = -500$ m. This pycno-
 815 cline depth corresponds to typical conditions offshore of the WAIS (i.e. neither warm
 816 nor cold) [51, 52]. In the following, we refer to warm forcing as constant forcing with
 817 $P_c = -400$ m, corresponding approximately to the shallowest recorded pycnocline
 818 depth [51]. Similarly, we refer to cold forcing as constant forcing with $P_c = -600$ m,
 819 corresponding approximately to the deepest recorded pycnocline depth [51]. The
 820 second initialization stage is performed independently for each value of M . The (M -
 821 dependent) state at the end of the second initialization stage (figure 3c) is then used
 822 as the initial condition in the following retreat simulations (figure 3).

823 Note that for a consistent estimate of SLR contributions from simulations with
 824 different values of M , we require similar initial conditions, chosen to be a grounding
 825 line at or near the seabed ridge crest. For $M \gtrsim 1.5$, the ice retreats irreversibly
 826 down the ridge during the second initialization stage. We therefore consider only M
 827 values smaller than this. In addition, we impose that a constant warm forcing applied
 828 to the shelf should initiate retreat (WAIS retreat was, in practice, hypothesised to

be initiated with forcing oscillating between warm and cold [11]); we found that for $M \lesssim 0.5$, no ice sheet retreat was initiated under warm forcing. Therefore, we restrict ourselves to the range $0.5 \leq M \leq 1.5$. Note that this restriction is consistent with our Bayesian framework: it is equivalent to setting the prior density to zero outside the range $0.5 \leq M \leq 1.5$, based on observational constraints.

During the second initialization stage, the ice shelf thins in response to applied melting, but the grounding line does not retreat (figure 3c). The mean melt rate after the second initialization stage is only weakly dependent on M (figure 3b). If the geometries at the end of the second initialization were identical for different values of M , the mean melt rate in the simulation with $M = 1.5$ would be 3 times as large as that with $M = 0.5$ (black dashed line in figure 3b); however, owing to temperature-depth effects, this value is only approximately 1.1 times (approximately 23.5 m year^{-1} in the $M = 1.5$ case versus approximately 21.3 m year^{-1} in the $M = 0.5$ case, see figure 3b). As the ice shelf thins in response to melting, it shallows, exposing it to colder ocean conditions, reducing melt rates sharply and restricting further thinning (the melt rate is proportional to $(T_a - T_f)^2$, which varies sharply with depth, particularly in the depth range occupied by the ice shelf in the second calibration phase, see figure 3d).

Stochastic forcing

Following the two stage initialization procedure outlined above, stochastic forcing is applied via ambient ocean conditions:

$$P_c(t, \mathcal{F}) = P_{c,0} + T(\mathcal{F}) + A\mathcal{R}(t) \quad (13)$$

where $P_{c,0} = -500 \text{ m}$ is the pycnocline depth in the second stage of the initialization procedure, $T(\mathcal{F})$ is a forcing-scenario-dependent (i.e. anthropogenic or counterfactual) trend (see below), A is the amplitude of random forcing, and $\mathcal{R}(t)$ is a first-order autoregressive process, containing the stochastic part of the forcing. In the results shown here, we use $A = 100 \text{ m}$, which agrees with observed internal variability in the Amundsen Sea [52]. In a first-order autoregressive time-series, the following value is decomposed into a component proportional to the current entry, whose constant of proportionality describes the persistence timescale of the variability, and an additive white-noise term. We take the same autocorrelation function as [35], with interdecadal-to-decadal timescales well represented.

Anthropogenic and counterfactual ensembles are distinguished via the trend $T(\mathcal{F})$: realizations of forcing from the counterfactual ensemble have no trend added to them, $T = 0 \text{ m}$; realizations of forcing in the anthropogenic ensemble have a linear trend, $T = A_0(t/100 \text{ yrs})$, where $A_0 = 100 \text{ m}$ is the per-century shallowing trend of the pycnocline (figure 2g).

Bootstrapping distributions of sea level rise

Each of the n realizations of forcing yields a parametrically-calibrated distribution of SLR for each time in the simulation. Thus, for any time and any SLR, we have n values of the distributions from both anthropogenic and counterfactual ensembles

875 (supplementary figure 5). An uncertainty estimate in the anthropogenic enhancement
876 ratio is constructed by bootstrapping these values – resampling from these n values
877 with replacement (here, we sample 1000 times); the resulting set yields a standard
878 deviation $\lambda = \lambda(SLR, t)$ for both anthropogenic and counterfactual ensembles (sup-
879 plementary figure 5). Using subscripts to denote the ensemble (that is, counterfactual
880 or anthropogenic), the upper bound shown in figure 4b–d is then computed as

881

882

883

884

$$\text{AER}_{\text{upper}} = \frac{\ell_{\text{anthro}} + \lambda_{\text{anthro}}}{\ell_{\text{counter}} - \lambda_{\text{counter}}} \quad (14)$$

885

886

887

888

889

890

where $\ell = \ell(SLR, t)$ is the probability density. Similarly, the lower bound is computed
as

891

892

$$\text{AER}_{\text{lower}} = \frac{\ell_{\text{anthro}} - \lambda_{\text{anthro}}}{\ell_{\text{counter}} + \lambda_{\text{counter}}} \quad (15)$$

891 References

892

893

894

895

896

897

898

899

900

901

902

903

904

905

906

907

908

909

910

911

912

913

914

915

916

917

918

919

920

- [1] Mougnot, J., Rignot, E. & Scheuchl, B. Sustained increase in ice discharge from the amundsen sea embayment, west antarctica, from 1973 to 2013. *Geophysical Research Letters* **41**, 1576–1584 (2014). doi:[10.1002/2013gl059069](https://doi.org/10.1002/2013gl059069).
- [2] Smith, B. *et al.* Pervasive ice sheet mass loss reflects competing ocean and atmosphere processes. *Science* **368**, 1239–1242 (2020). doi:[10.1126/science.aaz5845](https://doi.org/10.1126/science.aaz5845).
- [3] Rignot, E., Mougnot, J., Morlighem, M., Seroussi, H. & Scheuchl, B. Widespread, rapid grounding line retreat of pine island, thwaites, smith, and kohler glaciers, west antarctica, from 1992 to 2011. *Geophysical Research Letters* **41**, 3502–3509 (2014). doi:[10.1002/2014GL060140](https://doi.org/10.1002/2014GL060140).
- [4] IMBIE. Mass balance of the antarctic ice sheet from 1992 to 2017. *Nature* **558**, 219–222 (2018). doi:[10.1038/s41586-018-0179-y](https://doi.org/10.1038/s41586-018-0179-y).
- [5] Otosaka, I. N. *et al.* Mass balance of the greenland and antarctic ice sheets from 1992 to 2020. *Earth System Science Data* **15**, 1597–1616 (2023). doi:[10.5194/essd-15-1597-2023](https://doi.org/10.5194/essd-15-1597-2023).
- [6] Wouters, B., van de Wal, R. *et al.* Global sea-level budget 1993–present. *Earth System Science Data* **10**, 1551–1590 (2018). doi:[10.5194/essd-10-1551-2018](https://doi.org/10.5194/essd-10-1551-2018).
- [7] Edwards, T. L. *et al.* Projected land ice contributions to twenty-first-century sea level rise. *Nature* **593**, 74–82 (2021). doi:[10.1038/s41586-021-03302-y](https://doi.org/10.1038/s41586-021-03302-y).
- [8] Leiserowitz, A. Communicating the risks of global warming: American risk perceptions, affective images, and interpretive communities. *Creating a climate for change: Communicating climate change and facilitating social change* 44–63 (2007). doi:[10.1017/CBO9780511535871.005](https://doi.org/10.1017/CBO9780511535871.005).

- [9] Lehman, B., Thompson, J., Davis, S. & Carlson, J. M. Affective images of climate change. *Frontiers in psychology* **10**, 960 (2019). doi:[10.3389/fpsyg.2019.00960](https://doi.org/10.3389/fpsyg.2019.00960). 921
922
- [10] Meredith, M. M. *et al.* Polar regions. in: Ipcc special report on the ocean and cryosphere in a changing climate [h.-o. pörtner, d.c. roberts, v. masson-delmotte, p. zhai, m. tignor, e. poloczanska, k. mintenbeck, a. alegría, m. nicolai, a. okem, j. petzold, b. rama, n.m. weyer (eds.)] (2019). doi:[10.1017/9781009157964](https://doi.org/10.1017/9781009157964). 923
924
925
926
927
- [11] Smith, J. A. *et al.* Sub-ice-shelf sediments record history of twentieth-century retreat of pine island glacier. *Nature* **541**, 77–80 (2017). doi:[10.1038/nature20136](https://doi.org/10.1038/nature20136). 928
929
930
- [12] Steig, E. J., Ding, Q., Battisti, D. & Jenkins, A. Tropical forcing of circumpolar deep water inflow and outlet glacier thinning in the amundsen sea embayment, west antarctica. *Annals of Glaciology* **53**, 19–28 (2012). doi:[10.3189/2012AoG60A110](https://doi.org/10.3189/2012AoG60A110). 931
932
933
934
935
- [13] O’Connor, G. K., Holland, P. R., Steig, E. J., Dutrieux, P. & Hakim, G. J. Drivers and rarity of the strong 1940s westerly wind event over the amundsen sea, west antarctica. *The Cryosphere Discussions* **2023**, 1–26 (2023). doi:[10.5194/tc-2023-16](https://doi.org/10.5194/tc-2023-16). 936
937
938
939
940
- [14] Larter, R. D. *et al.* Reconstruction of changes in the amundsen sea and bellingshausen sea sector of the west antarctic ice sheet since the last glacial maximum. *Quaternary Science Reviews* **100**, 55–86 (2014). doi:[10.1016/j.quascirev.2013.10.016](https://doi.org/10.1016/j.quascirev.2013.10.016). 941
942
943
944
945
- [15] Holland, P. R. *et al.* Anthropogenic and internal drivers of wind changes over the amundsen sea, west antarctica, during the 20th and 21st centuries. *The Cryosphere* **16**, 5085–5105 (2022). doi:[10.5194/tc-16-5085-2022](https://doi.org/10.5194/tc-16-5085-2022). 946
947
948
949
- [16] De Rydt, J., Holland, P. R., Dutrieux, P. & Jenkins, A. Geometric and oceanographic controls on melting beneath pine island glacier. *J. Geophys. Res. Oceans* **119**, 2420–2438 (2014). doi:[10.1002/2013JC009513](https://doi.org/10.1002/2013JC009513). 950
951
952
- [17] Favier, L. *et al.* Retreat of pine island glacier controlled by marine ice-sheet instability. *Nature Climate Change* **4**, 117–121 (2014). doi:[10.1038/nclimate2094](https://doi.org/10.1038/nclimate2094). 953
954
955
- [18] Bett, D. T. *et al.* The impact of the amundsen sea freshwater balance on ocean melting of the west antarctic ice sheet. *Journal of Geophysical Research: Oceans* **125**, e2020JC016305 (2020). doi:[10.1029/2020JC016305](https://doi.org/10.1029/2020JC016305). 956
957
958
959
- [19] Lhermitte, S. *et al.* Damage accelerates ice shelf instability and mass loss in amundsen sea embayment. *Proceedings of the National Academy of Sciences* **117**, 24735–24741 (2020). doi:[10.1073/pnas.1912890117](https://doi.org/10.1073/pnas.1912890117). 960
961
962
963
- [20] Bradley, A., Bett, D., Dutrieux, P., De Rydt, J. & Holland, P. The influence of pine island ice shelf calving on basal melting. *Journal of Geophysical Research:* 964
965
966

- 967 *Oceans* **127**, e2022JC018621 (2022). doi:[10.1029/2022JC018621](https://doi.org/10.1029/2022JC018621).
- 968
- 969 [21] Holland, P. R., Bevan, S. L. & Luckman, A. J. Strong ocean melting feedback
970 during the recent retreat of thwaites glacier. *Geophysical Research Letters* **50**,
971 e2023GL103088 (2023). doi:[10.1029/2023GL103088](https://doi.org/10.1029/2023GL103088).
- 972
- 973 [22] Weertman, J. Stability of the junction of an ice sheet and an ice shelf. *Journal*
974 *of Glaciology* **13**, 3–11 (1974). doi:[10.3189/S0022143000023327](https://doi.org/10.3189/S0022143000023327).
- 975
- 976 [23] Schoof, C. Ice sheet grounding line dynamics: Steady states, stability, and
977 hysteresis. *Journal of Geophysical Research: Earth Surface* **112** (2007).
978 doi:[10.1029/2006JF000664](https://doi.org/10.1029/2006JF000664).
- 979
- 980 [24] Holland, P. R., Bracegirdle, T. J., Dutrieux, P., Jenkins, A. & Steig, E. J. West
981 antarctic ice loss influenced by internal climate variability and anthropogenic
982 forcing. *Nature Geoscience* **12**, 718–724 (2019). doi:[10.1038/s41561-019-0420-9](https://doi.org/10.1038/s41561-019-0420-9).
- 983
- 984 [25] Christianson, K. *et al.* Sensitivity of pine island glacier to observed ocean forcing.
985 *Geophysical Research Letters* **43**, 10–817 (2016). doi:[10.1002/2016GL070500](https://doi.org/10.1002/2016GL070500).
- 986
- 987 [26] Jenkins, A. *et al.* West antarctic ice sheet retreat in the amundsen sea driven by
988 decadal oceanic variability. *Nat. Geosci.* **11**, 733–738 (2018). doi:[10.1038/s41561-018-0207-4](https://doi.org/10.1038/s41561-018-0207-4).
- 989
- 990 [27] Christie, F. D., Steig, E. J., Gourmelen, N., Tett, S. F. & Bingham, R. G. Inter-
991 decadal climate variability induces differential ice response along pacific-facing
992 west antarctica. *Nature Communications* **14**, 93 (2023). doi:[10.1038/s41467-022-35471-3](https://doi.org/10.1038/s41467-022-35471-3).
- 993
- 994
- 995 [28] Naughten, K. A. *et al.* Simulated twentieth-century ocean warming in the amund-
996 sen sea, west antarctica. *Geophysical Research Letters* **49**, e2021GL094566 (2022).
997 doi:[10.1029/2021GL094566](https://doi.org/10.1029/2021GL094566).
- 998
- 999 [29] O'Connor, G. K., Steig, E. J. & Hakim, G. J. Strengthening southern hemi-
1000 sphere westerlies and amundsen sea low deepening over the 20th century revealed
1001 by proxy-data assimilation. *Geophysical Research Letters* **48**, e2021GL095999
1002 (2021). doi:[10.1029/2021GL095999](https://doi.org/10.1029/2021GL095999).
- 1003
- 1004 [30] Dalaiden, Q., Goosse, H., Rezsöhazy, J. & Thomas, E. R. Reconstructing
1005 atmospheric circulation and sea-ice extent in the west antarctic over the past
1006 200 years using data assimilation. *Climate Dynamics* **57**, 3479–3503 (2021).
1007 doi:[10.1007/s00382-021-05879-6](https://doi.org/10.1007/s00382-021-05879-6).
- 1008
- 1009 [31] Graham, S. *et al.* The social values at risk from sea-level rise. *Environmental*
1010 *Impact Assessment Review* **41**, 45–52 (2013). doi:[10.1016/j.eiar.2013.02.002](https://doi.org/10.1016/j.eiar.2013.02.002).
- 1011
- 1012

- [32] Hinkel, J. *et al.* Coastal flood damage and adaptation costs under 21st century sea-level rise. *Proceedings of the National Academy of Sciences* **111**, 3292–3297 (2014). doi:[10.1073/pnas.1222469111](https://doi.org/10.1073/pnas.1222469111). 1013
1014
1015
1016
- [33] Craft, C. *et al.* Forecasting the effects of accelerated sea-level rise on tidal marsh ecosystem services. *Frontiers in Ecology and the Environment* **7**, 73–78 (2009). doi:[10.1890/070219](https://doi.org/10.1890/070219). 1017
1018
1019
1020
- [34] IPCC. *Climate Change 2022: Impacts, Adaptation, and Vulnerability. Contribution of Working Group II to the Sixth Assessment Report of the Intergovernmental Panel on Climate Change* (Cambridge University Press, Cambridge, United Kingdom and New York, NY, USA, 2022). 1021
1022
1023
1024
- [35] Christian, J. E., Robel, A. A. & Catania, G. A probabilistic framework for quantifying the role of anthropogenic climate change in marine-terminating glacier retreats. *The Cryosphere* 1–28 (2022). doi:[10.5194/tc-16-2725-2022](https://doi.org/10.5194/tc-16-2725-2022). 1025
1026
1027
1028
- [36] Otto, F. E. Attribution of weather and climate events. *Annual Review of Environment and Resources* **42**, 627–646 (2017). doi:[10.1146/annurev-environ-102016-060847](https://doi.org/10.1146/annurev-environ-102016-060847). 1029
1030
1031
1032
- [37] Aschwanden, A., Bartholomäus, T. C., Brinkerhoff, D. J. & Truffer, M. Brief communication: A roadmap towards credible projections of ice sheet contribution to sea level. *The Cryosphere* **15**, 5705–5715 (2021). doi:[10.5194/tc-15-5705-2021](https://doi.org/10.5194/tc-15-5705-2021). 1033
1034
1035
1036
- [38] Nias, I. J., Cornford, S. L., Edwards, T. L., Gourmelen, N. & Payne, A. J. Assessing uncertainty in the dynamical ice response to ocean warming in the amundsen sea embayment, west antarctica. *Geophysical Research Letters* **46**, 11253–11260 (2019). doi:[10.1029/2019GL084941](https://doi.org/10.1029/2019GL084941). 1037
1038
1039
1040
1041
- [39] Nias, I. J., Nowicki, S., Felikson, D. & Loomis, B. Modeling the greenland ice sheet’s committed contribution to sea level during the 21st century. *Journal of Geophysical Research: Earth Surface* **128**, e2022JF006914 (2023). doi:[10.1029/2022jf006914](https://doi.org/10.1029/2022jf006914). 1042
1043
1044
1045
1046
- [40] Aschwanden, A. & Brinkerhoff, D. Calibrated mass loss predictions for the greenland ice sheet. *Geophysical Research Letters* **49**, e2022GL099058 (2022). doi:[10.1029/2022GL099058](https://doi.org/10.1029/2022GL099058). 1047
1048
1049
1050
- [41] Ritz, C. *et al.* Potential sea-level rise from antarctic ice-sheet instability constrained by observations. *Nature* **528**, 115–118 (2015). doi:[10.1038/nature16147](https://doi.org/10.1038/nature16147). 1051
1052
1053
- [42] Wernecke, A., Edwards, T. L., Nias, I. J., Holden, P. B. & Edwards, N. R. Spatial probabilistic calibration of a high-resolution amundsen sea embayment ice sheet model with satellite altimeter data. *The Cryosphere* **14**, 1459–1474 (2020). doi:[10.5194/tc-14-1459-2020](https://doi.org/10.5194/tc-14-1459-2020). 1054
1055
1056
1057
1058

- 1059 [43] Bevan, S. *et al.* Amundsen sea embayment ice-sheet mass-loss predictions to 2050
1060 calibrated using observations of velocity and elevation change. *J. Glaciol.* 1–11
1061 (2023). doi:[10.1017/jog.2023.57](https://doi.org/10.1017/jog.2023.57).
1062
- 1063 [44] Asay-Davis, X. S., Jourdain, N. C. & Nakayama, Y. Developments in simulating
1064 and parameterizing interactions between the southern ocean and the antarctic ice
1065 sheet. *Current Climate Change Reports* **3**, 316–329 (2017). doi:[10.1007/s40641-](https://doi.org/10.1007/s40641-017-0071-0)
1066 [017-0071-0](https://doi.org/10.1007/s40641-017-0071-0).
1067
- 1068 [45] Bradley, A. T., Rosie Williams, C., Jenkins, A. & Arthern, R. Asymptotic analysis
1069 of subglacial plumes in stratified environments. *Proceedings of the Royal Society*
1070 *A* **478**, 20210846 (2022). doi:[10.1098/rspa.2021.0846](https://doi.org/10.1098/rspa.2021.0846).
1071
- 1072 [46] Bradley, A. T., De Rydt, J., Bett, D. T., Dutrieux, P. & Holland, P. R. The
1073 ice dynamic and melting response of pine island ice shelf to calving. *Annals of*
1074 *Glaciology* 1–5 (2023). doi:[10.1017/aog.2023.24](https://doi.org/10.1017/aog.2023.24).
1075
- 1076 [47] Seroussi, H. *et al.* Continued retreat of thwaites glacier, west antarctica, controlled
1077 by bed topography and ocean circulation. *Geophys. Res. Lett.* **44**, 6191–6199
1078 (2017). doi:[10.1002/2017GL072910](https://doi.org/10.1002/2017GL072910).
1079
- 1080 [48] Snow, K. *et al.* The response of ice sheets to climate variability. *Geophys. Res.*
1081 *Lett.* **44**, 11,878–11,885 (2017). doi:[10.1002/2017GL075745](https://doi.org/10.1002/2017GL075745).
1082
- 1083 [49] De Rydt, J. & Gudmundsson, G. H. Coupled ice shelf-ocean modeling and com-
1084 plex grounding line retreat from a seabed ridge. *J. Geophys. Res. Earth Surf.*
1085 **121**, 865–880 (2016). doi:[10.1002/2015JF003791](https://doi.org/10.1002/2015JF003791).
1086
- 1087 [50] Favier, L. *et al.* Assessment of sub-shelf melting parameterisations using the
1088 ocean–ice-sheet coupled model nemo (v3. 6)–elmer/ice (v8. 3). *Geosci. Model*
1089 *Dev.* **12**, 2255–2283 (2019). doi:[10.5194/gmd-12-2255-2019](https://doi.org/10.5194/gmd-12-2255-2019).
1090
- 1091 [51] Webber, B. G. *et al.* Mechanisms driving variability in the ocean forc-
1092 ing of pine island glacier. *Nature communications* **8**, 14507 (2017).
1093 doi:[10.1038/ncomms14507](https://doi.org/10.1038/ncomms14507).
1094
- 1095 [52] Dutrieux, P. *et al.* Strong sensitivity of pine island ice-shelf melting to climatic
1096 variability. *Science* **343**, 174–178 (2014). doi:[10.1126/science.1244341](https://doi.org/10.1126/science.1244341).
1097
- 1098 [53] Jourdain, N. C., Mathiot, P., Burgard, C., Caillet, J. & Kittel, C. Ice shelf basal
1099 melt rates in the amundsen sea at the end of the 21st century. *Geophysical*
1100 *Research Letters* **49**, e2022GL100629 (2022). doi:[10.1029/2022GL100629](https://doi.org/10.1029/2022GL100629).
1101
- 1102 [54] Shepherd, A., Wingham, D. & Rignot, E. Warm ocean is eroding west antarctic
1103 ice sheet. *Geophysical Research Letters* **31** (2004). doi:[10.1029/2004GL021284](https://doi.org/10.1029/2004GL021284).
1104

- [55] Pritchard, H. *et al.* Antarctic ice-sheet loss driven by basal melting of ice shelves. *Nature* **484**, 502–505 (2012). doi:[10.1038/nature10968](https://doi.org/10.1038/nature10968). 1105
1106
- [56] Burgard, C., Jourdain, N. C., Reese, R., Jenkins, A. & Mathiot, P. An assessment of basal melt parameterisations for antarctic ice shelves. *The Cryosphere Discussions* **2022**, 1–56 (2022). URL <https://tc.copernicus.org/preprints/tc-2022-32/>. doi:[10.5194/tc-2022-32](https://doi.org/10.5194/tc-2022-32). 1107
1108
1109
1110
1111
- [57] Lazeroms, W. M., Jenkins, A., Gudmundsson, G. H. & Van De Wal, R. S. Modelling present-day basal melt rates for antarctic ice shelves using a parametrization of buoyant meltwater plumes. *The Cryosphere* **12**, 49–70 (2018). doi:[10.5194/tc-12-49-2018](https://doi.org/10.5194/tc-12-49-2018). 1112
1113
1114
1115
1116
- [58] Vargo, L. J. *et al.* Anthropogenic warming forces extreme annual glacier mass loss. *Nature Climate Change* **10**, 856–861 (2020). doi:[10.1038/s41558-020-0849-2](https://doi.org/10.1038/s41558-020-0849-2). 1117
1118
1119
- [59] Roe, G. H., Christian, J. E. & Marzeion, B. On the attribution of industrial-era glacier mass loss to anthropogenic climate change. *The Cryosphere* **15**, 1889–1905 (2021). doi:[10.5194/tc-15-1889-2021](https://doi.org/10.5194/tc-15-1889-2021). 1120
1121
1122
1123
- [60] Surawy-Stepney, T., Hogg, A. E., Cornford, S. L. & Davison, B. J. Episodic dynamic change linked to damage on the thwaites glacier ice tongue. *Nature Geoscience* 1–7 (2023). doi:[10.1038/s41561-022-01097-9](https://doi.org/10.1038/s41561-022-01097-9). 1124
1125
1126
1127
- [61] Liu, Y. *et al.* Ocean-driven thinning enhances iceberg calving and retreat of antarctic ice shelves. *Proceedings of the National Academy of Sciences* **112**, 3263–3268 (2015). doi:[10.1073/pnas.1415137112](https://doi.org/10.1073/pnas.1415137112). 1128
1129
1130
1131
- [62] DeConto, R. M. & Pollard, D. Contribution of antarctica to past and future sea-level rise. *Nature* **531**, 591–597 (2016). doi:[10.1038/nature17145](https://doi.org/10.1038/nature17145). 1132
1133
1134
- [63] Joughin, I., Smith, B. E. & Schoof, C. G. Regularized coulomb friction laws for ice sheet sliding: Application to pine island glacier, antarctica. *Geophysical research letters* **46**, 4764–4771 (2019). doi:[10.1029/2019GL082526](https://doi.org/10.1029/2019GL082526). 1135
1136
1137
- [64] Millstein, J. D., Minchew, B. M. & Pegler, S. S. Ice viscosity is more sensitive to stress than commonly assumed. *Communications Earth & Environment* **3**, 57 (2022). doi:[10.1038/s43247-022-00385-x](https://doi.org/10.1038/s43247-022-00385-x). 1138
1139
1140
1141
- [65] Seroussi, H. & Morlighem, M. Representation of basal melting at the grounding line in ice flow models. *The Cryosphere* **12**, 3085–3096 (2018). doi:[10.5194/tc-12-3085-2018](https://doi.org/10.5194/tc-12-3085-2018). 1142
1143
1144
1145
- [66] Vaughan, D. G. & Arthern, R. Why is it hard to predict the future of ice sheets? *Science* **315**, 1503–1504 (2007). doi:[10.1126/science.1141111](https://doi.org/10.1126/science.1141111). 1146
1147
1148
1149
1150

- 1151 [67] Robel, A. A., Seroussi, H. & Roe, G. H. Marine ice sheet instabil-
1152 ity amplifies and skews uncertainty in projections of future sea-level rise.
1153 *Proceedings of the National Academy of Sciences* **116**, 14887–14892 (2019).
1154 doi:[10.1073/pnas.1904822116](https://doi.org/10.1073/pnas.1904822116).
1155
- 1156 [68] Hawkins, E., Smith, R. S., Gregory, J. M. & Stainforth, D. A. Irreducible uncer-
1157 tainty in near-term climate projections. *Climate Dynamics* **46**, 3807–3819 (2016).
1158 doi:[10.1007/s00382-015-2806-8](https://doi.org/10.1007/s00382-015-2806-8).
1159
- 1160 [69] Stott, P. How climate change affects extreme weather events. *Science* **352**,
1161 1517–1518 (2016). doi:[10.1126/science.aaf7271](https://doi.org/10.1126/science.aaf7271).
1162
- 1163 [70] Cornford, S. L. *et al.* Results of the third marine ice sheet model intercomparison
1164 project (mismip+). *The Cryosphere* **14**, 2283–2301 (2020). doi:[10.5194/tc-14-2283-2020](https://doi.org/10.5194/tc-14-2283-2020).
1165
- 1166 [71] Jaynes, E. T. *Probability theory: The logic of science* (Cambridge university press,
1167 2003).
1168
- 1169 [72] Arthern, R. J. Exploring the use of transformation group priors and the method
1170 of maximum relative entropy for bayesian glaciological inversions. *Journal of*
1171 *Glaciology* **61**, 947–962 (2015). doi:[10.3189/2015JoG15J050](https://doi.org/10.3189/2015JoG15J050).
1172
- 1173 [73] Reese, R., Gudmundsson, G. H., Levermann, A. & Winkelmann, R. The far
1174 reach of ice-shelf thinning in antarctica. *Nature Climate Change* **8**, 53–57 (2018).
1175 doi:[10.1038/s41558-017-0020-x](https://doi.org/10.1038/s41558-017-0020-x).
1176
- 1177 [74] Fürst, J. J. *et al.* The safety band of antarctic ice shelves. *Nature Climate Change*
1178 **6**, 479–482 (2016). doi:[10.1038/nclimate2912](https://doi.org/10.1038/nclimate2912).
1179
- 1180 [75] Arthern, R. J. & Williams, C. R. The sensitivity of west antarctica to the sub-
1181 marine melting feedback. *Geophysical Research Letters* **44**, 2352–2359 (2017).
1182 doi:[10.1002/2017GL072514](https://doi.org/10.1002/2017GL072514).
1183
- 1184 [76] De Rydt, J., Reese, R., Paolo, F. S. & Gudmundsson, G. H. Drivers of pine island
1185 glacier speed-up between 1996 and 2016. *The Cryosphere* **15**, 113–132 (2021).
1186 doi:[10.5194/tc-15-113-2021](https://doi.org/10.5194/tc-15-113-2021).
1187
- 1188 [77] Medley, B. *et al.* Constraining the recent mass balance of pine island and thwaites
1189 glaciers, west antarctica, with airborne observations of snow accumulation. *The*
1190 *Cryosphere* **8**, 1375–1392 (2014). doi:[10.5194/tc-8-1375-2014](https://doi.org/10.5194/tc-8-1375-2014).
1191
- 1192 [78] Bradley, A. T., Arthern, R. J., Williams, C. R., Bett, D. T. & Byrne, J. Wavi.jl:
1193 Ice sheet modelling in julia.
1194
- 1195 [79] Goldberg, D. N. A variationally derived, depth-integrated approximation to a
1196 higher-order glaciological flow model. *Journal of Glaciology* **57**, 157–170 (2011).

doi:[10.3189/002214311795306763](https://doi.org/10.3189/002214311795306763). 1197

[80] Holland, P. R., Jenkins, A. & Holland, D. M. The response of ice shelf basal 1198
melting to variations in ocean temperature. *J. Clim.* **21**, 2558–2572 (2008). 1199
doi:[10.1175/2007JCLI1909.1](https://doi.org/10.1175/2007JCLI1909.1). 1200

[81] Jourdain, N. C. *et al.* A protocol for calculating basal melt rates in the 1201
ismip6 antarctic ice sheet projections. *The Cryosphere* **14**, 3111–3134 (2020). 1202
doi:[10.5194/tc-14-3111-2020](https://doi.org/10.5194/tc-14-3111-2020). 1203

[82] Marshall, J., Hill, C., Perelman, L. & Adcroft, A. Hydrostatic, quasi-hydrostatic, 1204
and nonhydrostatic ocean modeling. *Journal Geophys. Res. Oceans* **102**, 5733– 1205
5752 (1997). doi:[10.1029/96JC02776](https://doi.org/10.1029/96JC02776). 1206

[83] McDougall, T. J., Jackett, D. R., Wright, D. G. & Feistel, R. Accurate and 1207
computationally efficient algorithms for potential temperature and density of 1208
seawater. *J. Atmos. Ocean. Technol.* **20**, 730–741 (2003). doi:[10.1175/1520-0426\(2003\)20<730:ACEAF>2.0.CO;2](https://doi.org/10.1175/1520-0426(2003)20<730:ACEAF>2.0.CO;2). 1209

[84] Pacanowski, R. & Philander, S. Parameterization of vertical mixing in numer- 1210
ical models of tropical oceans. *J. Phys. Oceanogr.* **11**, 1443–1451 (1981). 1211
doi:[10.1175/1520-0485\(1981\)011<1443:POVMIN>2.0.CO;2](https://doi.org/10.1175/1520-0485(1981)011<1443:POVMIN>2.0.CO;2). 1212

[85] Holland, D. M. & Jenkins, A. Modeling thermodynamic ice–ocean interac- 1213
tions at the base of an ice shelf. *J. Phys. Oceanogr.* **29**, 1787–1800 (1999). 1214
doi:[10.1175/1520-0485\(1999\)029<1787:MTIOIA>2.0.CO;2](https://doi.org/10.1175/1520-0485(1999)029<1787:MTIOIA>2.0.CO;2). 1215

1216

1217

1218

1219

1220

1221

1222

1223

1224

1225

1226

1227

1228

1229

1230

1231

1232

1233

1234

1235

1236

1237

1238

1239

1240

1241

1242

1243
 1244
 1245
 1246
 1247
 1248
 1249
 1250
 1251
 1252
 1253
 1254
 1255
 1256
 1257
 1258
 1259
 1260
 1261
 1262
 1263
 1264
 1265
 1266
 1267
 1268
 1269
 1270
 1271
 1272
 1273
 1274
 1275
 1276
 1277
 1278
 1279
 1280
 1281
 1282
 1283
 1284
 1285
 1286
 1287
 1288

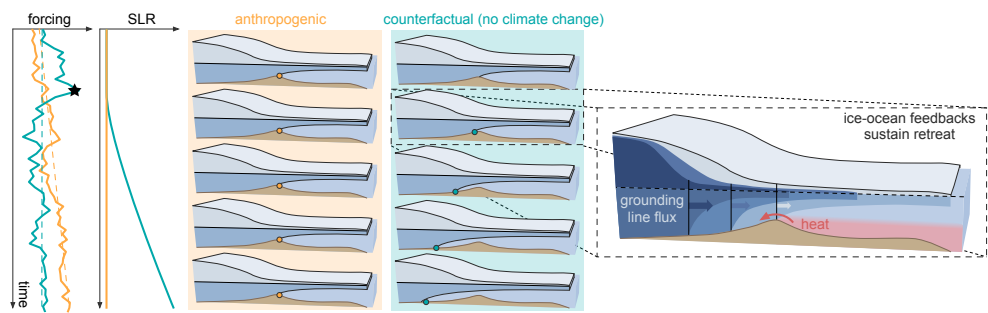


Fig. 1 Sea level rise from marine ice sheets is not necessarily an indicator of climate change. Schematic diagram demonstrating how an ice sheet configuration that remains stable under a realization of forcing including anthropogenic climate change (orange) may experience runaway retreat under a different, counterfactual realization of forcing with no anthropogenic climate change (green). As a result, grounding line retreat (filled dots in ice shelf configurations) and SLR are much higher in the counterfactual case. Once initiated (say, at the star), retreat from a topographic high is sustained by ice-ocean feedbacks.

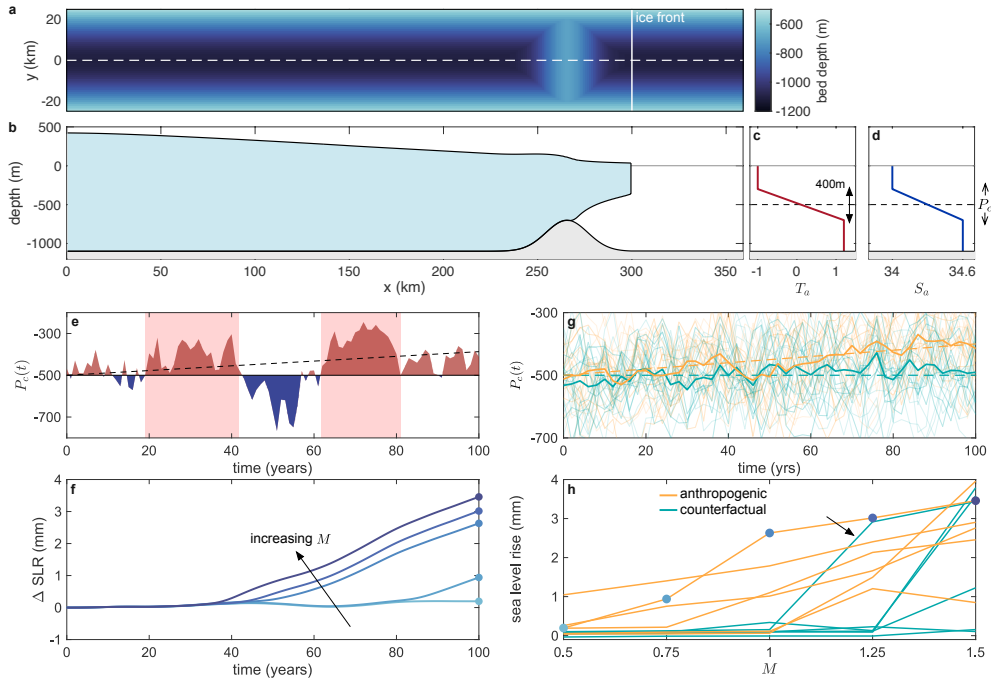
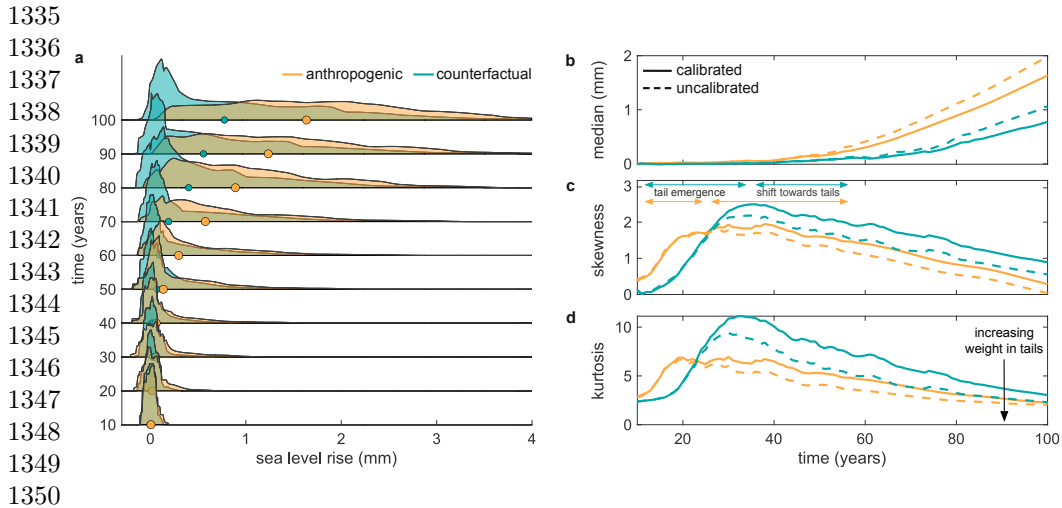
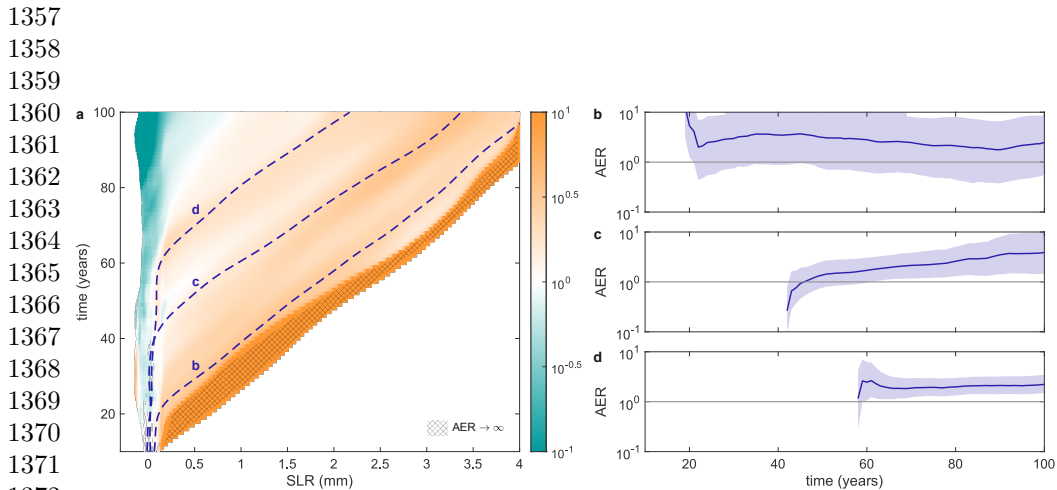


Fig. 2 Strong dependence of simulated marine ice sheet sea level rise on both forcing and model parameters. (a) Bathymetry (given by equation 7) of the marine ice sheet configuration. (b) Initial ice thickness along the dashed centerline in (a) for $M = 1$. The gray line indicates sea level. (c)–(d) Ambient temperature T_a (c) and salinity S_a (d) used in the parameterisation of melting and as restoring boundary conditions in the ocean model (methods). P_c denotes the pycnocline center, which parameterizes the piecewise linear forcing profiles and is oscillated to mimic variability. (e) Time evolution of a single realization of forcing and (f) corresponding SLR contributions for different values of $M \in \{0.5, 0.75, 1.0, 1.25, 1.5\}$ (the arrow indicates the direction of increasing M). Blue and red regions in (e) indicate whether the forcing is warmer (shallower pycnocline) or colder (deeper pycnocline) than during the calibration phase, where $P_c = -500$ m (black horizontal line), and shaded red regions indicate two prominent warm periods. The black dashed line indicates the 100 m/century anthropogenic trend in the pycnocline depth. (g) Time evolution of pycnocline centres P_c in all realizations of forcing. Here, orange curves correspond to forcing scenarios with an anthropogenic trend of a 100 m/century shallowing of the pycnocline, while green curves correspond to a counterfactual scenario, with no trend in the forcing (methods). In both cases, faint curves indicate individual ensemble members, while solid curves indicate ensemble means, and dashed lines indicate the externally imposed trend (the $T(\mathcal{F})$ term in equation (13)), i.e. 100m/century and 0m/century shallowing of the pycnocline in the anthropogenic and counterfactual cases, respectively. (h) SLR after 100 years as a function of M for a subset of the different realizations of forcing. Each line corresponds to an individual realization of forcing, and colors indicate whether the forcing is drawn from the anthropogenic (orange) or counterfactual (green) ensemble. Blue hue points correspond to the points shown in panel f. The arrow indicates the curve referred to as the ‘highlighted’ curve in the main text.

1289
1290
1291
1292
1293
1294
1295
1296
1297
1298
1299
1300
1301
1302
1303
1304
1305
1306
1307
1308
1309
1310
1311
1312
1313
1314
1315
1316
1317
1318
1319
1320
1321
1322
1323
1324
1325
1326
1327
1328
1329
1330
1331
1332
1333
1334



1351 **Fig. 3 Influence of anthropogenic forcing on distributions of sea level rise.** (a) Time
 1352 evolution (running bottom to top) of distributions of SLR from ensembles with an anthropogenic trend
 1353 in forcing (orange) and with a counterfactual trend (i.e. no-trend) in forcing (green). Filled markers
 1354 indicate the median of the distributions at the corresponding time. (b)–(d) Summary statistics of
 1355 the distributions in (a) as follows: (b) median, (c) skewness and (d) kurtosis. In each, the dashed
 1356 lines indicate the corresponding summary statistics for distributions obtained without parametric
 1357 calibration, obtained by assigning equal likelihood to each value of M .



1374 **Fig. 4 Signals of anthropogenic climate change in sea level rise from a synthetic marine**
 1375 **ice sheet.** (a) Contour plot of anthropogenic enhancement ratio (AER) as a function of time and
 1376 space, with colors as indicated by the colorbar. The hatched region indicates the area where AER
 1377 $\rightarrow \infty$. (b)–(d) Time evolution of AER (solid lines) along selected simulation trajectories of SLR,
 1378 corresponding to labelled lines in (a). The shaded region indicates the uncertainty in this metric,
 1379 obtained by bootstrapping values of distributions that result from individual realizations of forcing
 1380 (methods). Data are shown only for times where SLR > 0.1 mm for clarity.